Three-dimensional cascaded system analysis of a 50 µm pixel pitch wafer-scale CMOS active pixel sensor x-ray detector for digital breast tomosynthesis

Three-dimensional cascaded system analysis of a 50 μm pixel pitch wafer-scale CMOS active pixel sensor x-ray detector for digital breast tomosynthesis

C. Zhao[1], N. Vassiljev[2], A. C. Konstantinidis[3], R. D. Speller[2] and J. Kanicki[1]

[1] Solid-State Electronics Laboratory, Department of Electrical Engineering and Computer Science, University of Michigan, Ann Arbor, MI 48105, USA

[2] Department of Medical Physics and Biomedical Engineering, University College London, London WC1E 6BT, UK

[3] Diagnostic Radiology and Radiation Protection, Christie Medical Physics and Engineering, The Christie NHS Foundation Trust, Manchester, M20 4BX, UK

Email: kanicki@eecs.umich.edu

Abstract. High-resolution, low-noise x-ray detectors based on the complementary metal-oxide-semiconductor (CMOS) active pixel sensor (APS) technology have been developed and proposed for digital breast tomosynthesis (DBT). In this study, we evaluated the three-dimensional (3D) imaging performance of a 50 μm pixel pitch CMOS APS x-ray detector named DynAMITe (Dynamic Range Adjustable for Medical Imaging Technology). The two-dimensional (2D) angle-dependent modulation transfer function (MTF), normalized noise power spectrum (NNPS), and detective quantum efficiency (DQE) were experimentally characterized and modeled using the cascaded system analysis at oblique incident angles up to 30°. The cascaded system model was extended to the 3D spatial frequency space in combination with the filtered back-projection (FBP) reconstruction method to calculate the 3D and in-plane MTF, NNPS and DQE parameters. The results demonstrate that the beam obliquity blurs the 2D MTF and DQE in the high spatial frequency range. However, this effect can be eliminated after FBP image reconstruction. In addition, impacts of the image acquisition geometry and detector parameters were evaluated using the 3D cascaded system analysis for DBT. The result shows that a wider projection angle range (e.g. ±30°) improves the low spatial frequency (below 5 mm^{-1}) performance of the CMOS APS detector. In addition, to maintain a high spatial resolution for DBT, a focal spot size of smaller than 0.3 mm should be used. Theoretical analysis suggests that a pixelated scintillator in combination with the 50 μm pixel pitch CMOS APS detector could further improve the 3D image resolution. Finally, the 3D imaging performance of the CMOS APS and an indirect amorphous silicon (a-Si:H) thin-film

transistor (TFT) passive pixel sensor (PPS) detector was simulated and compared.

Keywords: CMOS active pixel sensor, x-ray detector, digital breast tomosynthesis, three-dimensional, cascaded system analysis, pixelated scintillator, detective quantum efficiency

1. Introduction

High performance x-ray detectors based on the complementary metal-oxide-semiconductor (CMOS) active pixel sensor (APS) have been recently studied for digital breast tomosynthesis (DBT) (Naday *et al* 2010, Patel *et al* 2012, Zhao *et al* 2015a, 2015b, Choi *et al* 2012, Peters *et al* 2016, Park *et al* 2014, Kim *et al* 2016). In comparison to conventional DBT systems based on amorphous silicon (a-Si:H) thin-film transistor (TFT) passive pixel sensor (PPS), the advantages of CMOS APS detectors are the smaller pixel pitch (40 – 75 μm), low electronic noise (50 – 165 e^-) and faster frame rate (20 – 30 fps) (Bohndiek *et al* 2009, Esposito *et al* 2011, 2014, Konstantinidis *et al* 2013). The high pixel resolution and low noise floor of CMOS APS detectors improves the two-dimensional (2D) imaging performance in comparison to a-Si:H TFT PPS detectors especially in high spatial frequency range (above 5 mm^{-1}) (Choi *et al* 2012, Patel *et al* 2012, Zhao *et al* 2015a, 2015b, Peters *et al* 2016). The analysis of reconstructed tomographic images show benefits of resolving subtle microcalcifications, as early indicators of breast cancer, using a 75 μm pixel pitch CMOS APS detector (Park *et al* 2014, Kim *et al* 2016). In addition, high dynamic range can be achieved using the CMOS APS detectors by switching between high full well (HFW) and low full well (LFW) modes (Konstantinidis *et al* 2012b, Patel *et al* 2012, Jiang *et al* 2016). It is clear that CMOS APS detectors are adequate for both full field digital mammography (FFDM) in the HFW mode and DBT in the LFW mode (Peters *et al* 2016).

Up to now, most studies focus on CMOS APS detector evaluation by measuring the one-dimensional (1D) or 2D modulation transfer function (MTF), noise power spectrum (NPS) and detective quantum efficiency (DQE) using a single x-ray projection at the zero-degree incident angle (perpendicular to the detector). Nevertheless, since DBT is a quasi-three-dimensional (3D) imaging technology, the DBT image quality is influenced by the system geometry and reconstruction algorithms (Sechopoulos 2013a, 2013b). Therefore, the 3D imaging performance should be evaluated for the CMOS APS detectors. However, it is difficult to empirically investigate the 3D image quality. To deal with this issue, the 3D cascaded system analysis for CMOS APS detectors was developed and is presented in this study.

Cascaded system analysis can accurately model the signal and noise propagation and blurring within a linear x-ray imaging system (Siewerdsen *et al* 1997, Vedantham *et al* 2004). Previously, 3D cascaded system analysis models have been developed and validated for both cone-beam computed tomography (CT) and DBT (Tward and Siewerdsen 2008, Zhao and Zhao 2008b, Zhao *et al* 2009, Hu and Zhao 2014, Siewerdsen and Jaffray 2003, Gang *et al* 2011, 2012). We have already reported a 2D cascaded system analysis model for a 50 μm pixel pitch CMOS APS detector named DynAMITe (Zhao *et al* 2015b). In this study, the previously developed 2D cascaded system model is extended to the 3D spatial frequency space. To implement the 3D cascaded system analysis, first the 2D MTF, NPS and DQE characteristics of the DynAMITe detector are measured and simulated at various projection angles (θ_i) ranging from 0 to 30°. This angle range covers the typical projection angles currently used for DBT systems (Sechopoulos 2013a). Then the filtered back-projection (FBP) reconstruction is used to convert the 2D MTF, NPS and DQE at each θ_i to the 3D spatial frequency domain (f_x, f_y, f_z). The FBP is a standard image reconstruction method currently used for clinically approved Hologic Selenia Dimensions and Siemens MAMMOMAT Inspiration DBT commercial systems (Sechopoulos 2013a). The implemented 3D cascaded system model is used to investigate the impacts of projection angle range, mean glandular dose (MGD), fiber optic plate optical coupling efficiency, focal spot blurring effect, pixel size and scintillator pixilation on the 3D imaging performance of the CMOS APS detector.

2. Materials and Methods

2.1. Experimental setup

The wafer-scale (12.8 cm × 13.1 cm) x-ray detector used in this study (named DynAMITe: Dynamic Range Adjustable for Medical Imaging Technology) is based on a three-transistor (3-T) CMOS APS pixel architecture (Esposito *et al* 2011, Konstantinidis *et al* 2012a, Esposito *et al* 2014). DynAMITe can operate both in a high dynamic range (68 dB), full pixel mode (P mode, 100 µm pixel pitch) and a low dynamic range (65 dB), subpixel mode (SP mode, 50 µm pixel pitch). To realize a high image resolution, the SP mode with a conversion gain of around 0.02 DN/e^- and maximum frame rate of 30 frames per second (fps) is used for DBT (Zhao *et al* 2015b). The detector is covered by a high resolution Thallium-doped cesium iodide (CsI:Tl) scintillator (150 µm thick) in combination with a fiber optic plate (FOP) (Zhao *et al* 2015b).

During a DBT scan, multiple projection images are collected at oblique projection angles. Oblique incident of x-ray photons on the detector will lead to resolution loss (MTF degradation at high spatial frequencies) (Mainprize *et al* 2006). It was also established that the off-axis incident x-ray beams do not affect the NPS (Hajdok and Cunningham 2004). Thus, DQE will be degraded by the square of MTF term. Therefore, it is important to evaluate experimentally the detector 2D MTF, NPS and DQE at oblique incident angles.

The angle-dependent 2D imaging performance of the DynAMITe detector was characterized by measuring the MTF, NPS and DQE parameters at oblique x-ray incident angles. As shown in Figure 1, a tomosynthesis bench-top system with a rotary stage was used to rotate the detector from 0 to 30° (incident x-ray beam is perpendicular to the detector at 0°). The detector is angulated together with the rotary stage, while the x-ray source is stationary. The x-ray source to detector distance is 65 cm and the center of rotation is located at the detector surface. This setup is empirically equivalent to a typical DBT system with a rotating x-ray source and fixed detector.

The used x-ray source was a tungsten (W) anode with an inherent aluminum (Al) filtration of 1.4 mm and a focal spot size of 3 mm. An external filtration of 1.1 mm Al was added to reach a total filtration of 2.5 mm Al and half value layer of around 0.83 mm Al according to the IEC standard for mammography (IEC 62220-1-2: 2007). A tube voltage of 28 kVp with a mean x-ray fluence per air kerma ratio ($\bar{q}_0/K_a$) of 7009 x-rays mm^{-2} µGy^{-1} was used (Zhao *et al* 2015b). The air kerma was fixed at K_a = 20 µGy for all projection angles. A sufficient large K_a value was used here to enhance the impact of oblique incident angles on the 2D detector performance.

The tilted edge technique was used to measure the 1D (horizontal and vertical) MTF of the

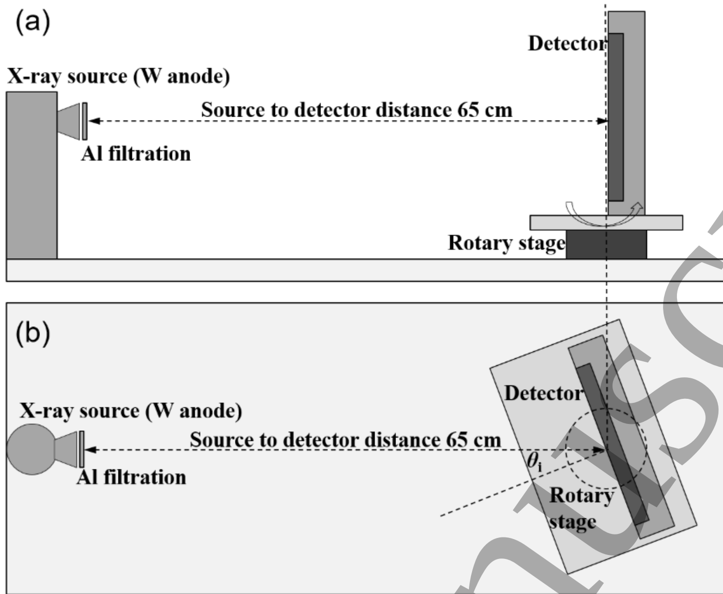

Figure 1. (a) Side-view and (b) top-view schematics of the bench-top system used to characterize the detector MTF, NNPS and DQE parameters. The detector is located on top of a rotary stage with a distance of 65 cm to the x-ray source.

DynAMITe detector at each projection angle θ_i (Samei *et al* 1998). A polished W edge plate was attached to the detector surface at a small tilted angle (1.5 - 3°) with respect to the detector rows or columns (Konstantinidis *et al* 2013, Zhao *et al* 2015b). At oblique projection angles, partial transmission of x-ray photons through the edge may affect the MTF. This is considered as a source of uncertainty in this study. At each projection angle, a number of raw edge images (N_{edge} = 20) and flat field images (N_{flat} = 10) were captured at fixed K_a = 20 μGy (measured at zero degree projection angle) to reduce the random noise. Since the CMOS APS x-ray detector is based on crystalline silicon (c-Si) technology, the bulk and interface traps are negligible resulting in a small image lag of <0.1% (Zentai 2011). Additional 10 frames of dark images (N_{dark} = 10) were also collected for raw image correction. The edge images were corrected by a standard gain and offset correction algorithm to remove the fixed pattern noise. Then a second order polynomial fit was applied on the corrected test images to eliminate the low spatial frequency trends arising from a non-uniform x-ray field that could possibly affect the MTF at low spatial frequencies (Konstantinidis *et al* 2011, IEC 62220-1-2: 2007). At each θ_i, an averaged oversampled edge spread function (ESF) was extracted from seven consecutive rows or columns of the corrected edge image (i.e. seven oversampled ESF profile). Then the averaged ESF was differentiated to obtain the line spread function (LSF). The 1D presampling MTF in either x (horizontal MTF(u)) or y direction (vertical MTF(v)) was calculated from the fast Fourier transform (FFT) of the oversampled LSF (Fujita *et al* 1992, Konstantinidis *et al* 2013, Zhao *et al* 2015b). The horizontal presampling MTF at θ_i is given by

$$MTF(u,\theta_i) = \left| FT\left\{ LSF(x,\theta_i) \right\} \right| = \left| FFT\left\{ \frac{\partial}{\partial x}\left[ESF(x,\theta_i) \right] \right\} \right|. \tag{1}$$

After that, the same process was repeated to measure the vertical presampling MTF at each θ_i, i.e.

MTF(v, θ_i) by rotating the tilted edge by 90°. We consider the rotatory plane is parallel to the x direction (i.e. the detector rotated horizontally).

The MTF component associated with the beam obliquity is given by

$$MTF_{ob}(u,\theta_i) = MTF(u,\theta_i)/MTF(u,0). \tag{2}$$

The NPS was measured from the gain and offset corrected flat-field images following the IEC standard (IEC 62220-1-2: 2007). The 2D NPS profile at each θ_i can be calculated by

$$NPS(u,v,\theta_i) = \frac{\Delta x \cdot \Delta y}{M \cdot N_x \cdot N_y} \sum_{j=1}^{M} \left| FFT\left[I(x_j, y_j, \theta_i) - S(x_j, y_j, \theta_i) \right] \right|^2, \tag{3}$$

where $I(x_j, y_j, \theta_i)$ is the corrected flat-field image at θ_i within a 256 × 256 region of interest (ROI), $S(x_j, y_j, \theta_i)$ is a 2D second order polynomial fit for $I(x_j, y_j, \theta_i)$ to remove the low frequency trends, Δx and Δy are the pixel pitches in x and y directions ($\Delta x = \Delta y = 50$ μm), M is the number of ROIs ($M = 243$ to reach at least three million independent pixels (IEC 62220-1-2: 2007)), N_x and N_y are the number of columns and rows in each ROI ($N_x = N_y = 256$) (IEC 62220-1-2: 2007, Konstantinidis *et al* 2013, Zhao *et al* 2015b). The 1D horizontal (NPS(u)) and vertical NPS (NPS(v)) were extracted and averaged from seven lines on either side of zero spatial frequency. The horizontal normalized NPS (NNPS) was calculated by $NNPS(u, \theta_i) = NPS(u, \theta_i) / d^2$, where d is the mean pixel signal in digital number (DN). The same process was used for vertical NNPS(v, θ_i).

The 1D DQE at each θ_i was calculated using the measured MTF and NNPS data. For instance, the horizontal DQE at θ_i is given by

$$DQE(u,\theta_i) = \frac{MTF^2(u,\theta_i)}{\overline{q_0} \cdot NNPS(u,\theta_i)}, \tag{4}$$

where $\overline{q_0}$ is the mean x-ray fluence measured at $\theta_i = 0$ ($\overline{q_0}$= 7009 x-rays mm^{-2} μGy × 20 μGy = 1.402 × 10^5 x-rays mm^{-2}). Taking into account the fact that $\overline{q_0}$ is angular dependent, calculated zero frequency DQE(0) at θ_i is expected to be reduced by a factor of cos(θ_i). Although q_0 is spatial variant, we consider that the mean value of $\overline{q_0}$ over a large area is approximately constant.

2.2. Three-dimensional cascaded system analysis

Cascaded system analysis can be used to describe the signal and noise performance of an x-ray imaging system (Siewerdsen *et al* 1997, Vedantham *et al* 2004, Zhao and Kanicki 2014, Zhao *et al* 2015a). The system signal and noise is cascaded separately through a series of gain and blurring stages. In a previous study, we have developed a 9-stage cascaded system analysis model for the DynAMITe CMOS APS x-ray detector with signal and noise nonlinearity included (Zhao *et al* 2015b). The model was used to study the 2D imaging performance of the DynAMITe detector. It was demonstrated that a high spatial resolution of 10 mm^{-1} can be achieved using the DynAMITe detector with 50 μm pixel pitch (Zhao *et al* 2015b). In this study, the validated 2D cascaded system analysis model is extended to 3D in combination with the FBP reconstruction method (Zhao and Zhao 2008b, Gang *et al* 2011, Tward and Siewerdsen 2008). This 3D model previously validated, using the Siemens MAMMOMAT Inspiration direct conversion a-Se detector with a-Si:H TFT PPS readout under DBT conditions (Zhao *et al* 2009), is expected to accurately predict the 3D imaging performance of the CMOS APS detector.

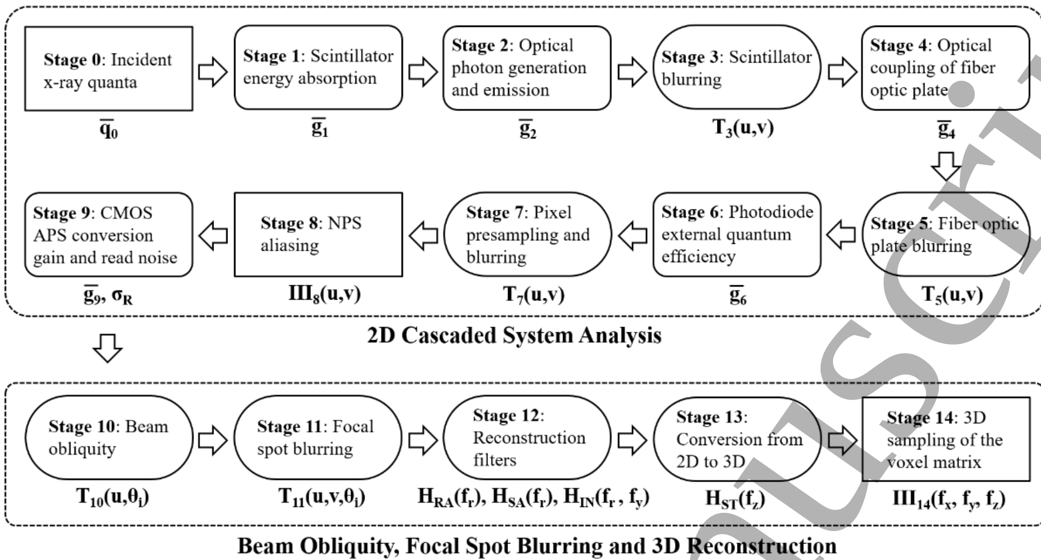

Figure 2. Illustration of the 3D cascaded system analysis. Stage 0 – 9 describes the 2D cascaded system model for the CMOS APS x-ray detector. Stage 10 – 14 describes the beam obliquity, focal spot blurring effect and filtered back-projection reconstruction.

A complete flowchart of the 3D cascaded system model is described in Figure 2.

Stage 0 – 3 includes the x-ray energy absorption (gain: $\overline{g_1}$) from the incident x-ray fluence ($\overline{q_0}$), optical photon generation and emission (gain: $\overline{g_2}$) and image blurring ($T_3(u,v)$) in the CsI:Tl scintillator, where u and v are the spatial frequencies in x and y directions, respectively. A 2D Lorentz fit was used to approximate the scintillator blurring effect, i.e. $T_3(\mathrm{u,v}) \approx (1+H_3(u^2+v^2))^{-1}$, where H_3 = 0.26. We assume the scintillator is uniform with isotropic optical properties on x and y directions in this study.

In this study, the impact of oblique x-ray incident angles is considered. At an oblique angle θ_i, the x-ray fluence is modified as $\overline{q_0}(\theta_\mathrm{i}) = \overline{q_0}\cdot \cos(\theta_\mathrm{i})$. The scintillator x-ray energy absorption efficiency (EAE) at θ_i is given by

$$\overline{g_1}(\theta_i) = EAE = \frac{\int_0^{E_{\max}} \Phi_0(E)\cdot T_0(E)\cdot E\cdot\left(\dfrac{\mu_{en}(E)}{\mu(E)}\right)\cdot\left(1-e^{-\mu(E)t/\cos\theta_i}\right)\cdot dE}{\int_0^{E_{\max}} \Phi_0(E)\cdot E\cdot dE}, \qquad (5)$$

where $\Phi_0(E)$ is the x-ray energy spectrum, $T_0(E)$ is the transmission (~0.9) of the scintillator protection layer, $t/\cos(\theta_\mathrm{i})$ is the optical path in the scintillator with a thickness of t =150 μm, $\mu(E)$ and $\mu_{\mathrm{en}}(E)$ are the linear attenuation and energy absorption coefficients of the scintillator, respectively. $\overline{g_1}(\theta_\mathrm{i} = 0)$ is around 0.56.

The mean light output (number of optical photons) per absorbed x-ray photon at θ_i can be described by

$$\overline{g_2}(\theta_i)=\frac{\int_0^{E_{\max}}\sum_z \Phi_0(E)\cdot\left(e^{-\mu(E)(t-z)/\cos\theta_i}\right)\cdot\left(1-e^{-\mu(E)\Delta z/\cos\theta_i}\right)\eta_{opt}\cdot E\cdot\eta_{esc}(z)dE}{\int_0^{E_{\max}}\Phi_0(E)\cdot T_0(E)\cdot\left(1-e^{-\mu(E)t/\cos\theta_i}\right)dE}, \tag{6}$$

where η_{opt} is the output yield of scintillator ($\eta_{\text{opt}} \approx 58$ photons/keV) and $\eta_{\text{esc}}(z)$ gives the fraction of generated photons at the vertical distance z to the bottom interface that can escape from the scintillator. The $\eta_{\text{opt}}\cdot E\cdot\eta_{\text{esc}}(z)$ represents the light output in number of escaped optical photons per absorbed x-ray quanta of energy E at position z in the scintillator (Vedantham *et al* 2004, Zhao *et al* 2015a, 2015b). The calculated $\overline{g_2}(\theta_{\text{i}} = 0)$ is around 580.

We assume that the oblique incident angles will not influence the stages that follows, since the optical path (moving direction) of the optical photons escaped from the scintillator is random.

As shown in equation (2), the MTF component associated with beam angulation (MTF_{ob}) is empirically defined as MTF(u,0)/MTF(u,θ_{i}). At each projection angle, stage 3 may be modified by MTF_{ob}. However, it has been reported (Hajdok and Cunningham 2004, Mainprize *et al* 2006, Hu and Zhao 2014) and supported by the experimental data collected in this study that the beam obliquity only has a major impact on the system MTF but not on NNPS. Therefore, the beam obliquity can be considered as a post-readout stage (stage 10) that only affects MTF after the 2D cascaded system analysis of the CMOS APS detector.

Stage 4 – 5 describes the optical coupling efficiency (gain: $\overline{g_4}$ ~ 0.4) and blurring ($T_5(u,v)$) by the fiber optic plate. The optical coupling efficiency is defined by the fiber optic numerical aperture, fiber optic core transmittance, Fresnel reflection, and fill factor (Hejazi and Trauernicht 1997, Jain *et al* 2011) with details described elsewhere (Zhao *et al* 2015b). The impact of optical coupling efficiency on performance metrics is independent of x-ray tube angulation. The direct deposition of scintillator on top of photodiode surface could improve the optical coupling efficiency and reduce the blurring.

Stage 6 gives the photodiode external quantum efficiency (gain: $\overline{g_6}$ ~ 0.6).

Stage 7 is a pixel presampling and deterministic blurring stage ($T_7(u,v)$) associated with the pixel pitch (a_{pix} = 50 μm).

Stage 8 describes the NPS aliasing effect using a Fourier transform of the sampling grid (comb function) ($III_8(u,v)$).

Stage 9 includes the CMOS APS conversion gain (gain: $\overline{g_9}$), additive electronic noise (σ_{R}) and detector signal and noise nonlinearity. $\overline{g_9}$ is around 0.022 – 0.025 DN/e^- due to the signal and noise nonlinearity, while σ_{R} is as low as 150 e^- (Zhao *et al* 2015b).

The output of stage 9 gives the detector 2D MTF(u,v), NNPS(u,v) and DQE(u,v) parameters at the zero projection angle. Details of the 2D cascaded system analysis for the DynAMITe CMOS APS detector were described elsewhere (Zhao *et al* 2015b).

Stage 10: Beam obliquity. The impact of oblique incident angles (θ_{i}) on MTF is included in this stage to describe the MTF blurring ($T_{10}(u,\theta_{\text{i}})$). It should be noted that $T_{10}(u,\theta_{\text{i}})$ only affects the MTF on the direction of rotation (x or u direction). The transfer function of the oblique incident angle blurring stage can be calculated by integrating the Fourier domain optical transfer function over the spectrum (Mainprize *et al* 2006)

$$T_{10}(u,\theta_i) = MTF_{ob}(u,\theta_i) = \frac{\left|\int E\,\frac{1-\exp\left(-\mu(E)t/\cos\theta_i - i2\pi ut\tan\theta_i\right)}{1+i2\pi u\sin\theta_i/\mu(E)}\,\Phi_0(E)dE\right|}{\int E\left[1-\exp\left(-\frac{\mu(E)t}{\cos\theta_i}\right)\right]\Phi_0(E)dE}. \tag{7}$$

The angle-dependent detector 2D MTF is given by MTF(u,v,θ_i) = MTF(u,v) × $T_{10}(u,\theta_i)$. The signal and noise power spectra are $\Psi_{10}(u,v,\theta_i)$ = MTF(u,v,θ_i) and $S_{10}(u,v,\theta_i)$ = NNPS(u,v,θ_i), respectively. The log-normalization has been taken into account during the normalization of NPS (Tward and Siewerdsen 2008).

Stage 11: Focal spot blurring. It was reported that the focal spot blurring can be the dominant system blurring factor for x-ray detectors with a pixel pitch smaller than 100 μm operated in the DBT mode (Zhao and Zhao 2008a). In general, there are two focal spot blurring components that need to be considered: the focal spot size (a_f) and the focal spot travel distance during a single x-ray projection. Since the CMOS APS detector is operated in a step-and-shoot tube motion mode, the focal spot travel distance can be neglected. Only the focal spot size is considered in this work. The focal spot size blurring transfer function can be determined by (Zhou *et al* 2007)

$$T_{11}(u,v,\theta_i) = \left|\text{sinc }(a_f(\theta_i)\cdot u)\times\text{sinc }(a_f(\theta_i)\cdot v)\right|, \tag{8}$$

where the focal spot size projected on the detector surface at projection angle θ_i is given by

$$a_f(\theta_i) = a_{fs}\cdot d_2/(d_1\cdot\cos\theta_i), \tag{9}$$

where a_{fs} is the source output focal spot size, d_1 is the distance of x-ray source to the center of rotation, d_2 is the distance of detector to the center of rotation at $\theta_i = 0$. We used d_1 = 61 cm and d_2 = 4 cm in the 3D cascaded system analysis. The impact of a_{fs} in the range of 0 to 3 mm is evaluated and discussed in Section 3.5. In our experiments, the relatively large focal spot size (3 mm) was not expected to affect the measured 2D MTF as both the center of rotation and the W plate are located at the detector surface (i.e. $d_2 = 0$).

The signal and noise power spectra at stage 11 are given by

$$\psi_{11}(u,v,\theta_i) = \psi_{10}(u,v,\theta_i)\times T_{11}(u,v,\theta_i), \tag{10}$$

$$S_{11}(u,v,\theta_i) = S_{10}(u,v,\theta_i). \tag{11}$$

As the focal spot blurring only affects the signal spectrum (MTF) without any impact on the NPS (Zhao and Zhao 2008b), it would be expected to have a significant influence on DQE.

Stage 12: Reconstruction filters. This stage includes the ramp (H_{RA}), spectrum apodization (H_{SA}) and interpolation filters (H_{IN}) that are used for FBP. Before applying the filters to the signal and noise power spectra, $\Psi_{11}(u,v,\theta_i)$ and $S_{11}(u,v,\theta_i)$ should be converted to the 3D space coordinated by (f_r, f_y, θ_i). The coordinates (f_r, f_y, θ_i) represents the tilted plane at θ_i perpendicular to the projection x-ray beam, while (u,v) gives the detector surface plane. The coordinates (f_r, θ_i) define the DBT system rotational plane. The relationship between (f_r, f_y, θ_i) and (u,v,θ_i) is described as $f_r = u/\cos(\theta_i) \approx u$ and $f_y = v$. In this paper, f_r can be approximated by u, since those large f_r values at wide θ_i will be filtered by the slice thickness filter to be discussed in Stage 13.

The ramp filter is a high-pass filter with the amplitude proportional to $|f_r|$. It is used to compensate the non-uniform spoke density at each f_r given by $N / (\theta \cdot f_r)$, where N (= 21 views) is the number of projection views and θ is the total angle range (e.g. θ = 40° for an incident angle range of ±20°). Without the ramp filter, it was found that the 3D MTF drops rapidly because of the normalization by the spoke density (Zhao and Zhao 2008b). The ramp filter is only applied to the f_r direction: (Zhao and Zhao 2008b)

$$H_{RA}(f_r) = 2\tan(\theta)\frac{|f_r|}{f_{r,Nyq}}, \quad |f_r| \le f_{r,Nyq} \tag{12}$$

where $f_{r,Nyq}$ is the Nyquist frequency on the f_r direction. For the DynAMITe detector with a 50 μm, $f_{r,Nyq}$ is 10 mm^{-1}.

The spectrum apodization filter is a smoothing low-pass filter to eliminate the high frequency noise given by (Zhao and Zhao 2008b, Hu and Zhao 2011)

$$H_{SA}(f_r) = 0.5\left[1+\cos\left(\frac{\pi f_r}{A f_{r,Nyq}}\right)\right], \quad |f_r| \le f_{r,Nyq} \tag{13}$$

where A defines the window width. A = 1.5 is used in the calculation (Zhao and Zhao 2008b), which will result in H_{SA} = 0.25 at $f_r = f_{r,Nyq}$ = 10 mm^{-1}. $H_{RA}(f_r)$ and $H_{SA}(f_r)$ duplicate at $f_r \pm n \cdot 2f_{r,Nyq}$ (n is an integer), if $|f_r| > f_{r,Nyq}$.

The 2D interpolation filter is used to approximate a continuous image, where the projection signal is located at the center of a pixel (Tward and Siewerdsen 2008):

$$H_{IN}(f_r, f_y) = \mathrm{sinc}(a_{pix} f_r)^2 \mathrm{sinc}(a_{pix} f_y)^2. \tag{14}$$

The signal and noise power spectra at stage 12 are given by (Zhao and Zhao 2008b, Tward and Siewerdsen 2008)

$$\psi_{12}(f_r, f_y, \theta_i) = \psi_{11}(f_r, f_y, \theta_i) \times H_{RA}(f_r) \times H_{SA}(f_r) \times H_{IN}(f_r, f_y), \tag{15}$$

$$S_{12}(f_r, f_y, \theta_i) = S_{11}(f_r, f_y, \theta_i) \times \left[H_{RA}(f_r) \times H_{SA}(f_r) \times H_{IN}(f_r, f_y)\right]^2. \tag{16}$$

Stage 13: Conversion from 2D to 3D. Using the FBP reconstruction method, the filtered Ψ_{12} and S_{12} planes at each θ_i will be reconstructed to the 3D frequency domain with the Cartesian coordinates of (f_x, f_y, f_z), where the (f_x, f_y) spatial frequency planes are parallel to the detector surface (u, v) and f_z is perpendicular to the detector. The typical reconstruction slice thickness (d_z) is around 1mm for DBT corresponding to $f_{z,Nyq} = 1/(2d_z)$ = 0.5 mm^{-1}. As discussed in stage 14, the z-direction 3D NPS aliasing (occurs at $f_z = n \cdot 2f_{z,Nyq}$) will dramatically increase the NPS at high f_r and f_y values. To prevent this effect, a slice thickness filter ($H_{ST}(f_z)$) should be added to limit the z-direction aliasing. H_{ST} is given by (Zhao and Zhao 2008b)

$$H_{ST}(f_z) = \begin{cases} 0.5\left[1+\cos\left(\frac{\pi f_z}{B f_{r,Nyq}}\right)\right], & |f_z| \le B f_{r,Nyq} \text{ and } |f_z| \le \tan(\theta) f_{r,Nyq} \\ 0 & \text{elsewhere} \end{cases} \tag{17}$$

where B is a parameter controling the width of the filter. In the calculation, B = 0.05 is used such that

$B \cdot f_{r,Nyq} = f_{z,Nyq} = 0.5$ mm^{-1}. In other words, MTF and NPS components at z-frequencies $f_z > f_{z,Nyq}$ are removed. Hence, the z-direction NPS aliasing will not affect the 3D imaging performance.

The 3D signal spectrum and NPS are given by (Zhao and Zhao 2008b)

$$\psi_{13}(f_r, f_y, \theta_i) = \frac{N}{\theta f_r} \times \psi_{12}(f_r, f_y, \theta_i) \times H_{ST}(f_z), \tag{18}$$

$$S_{13}(f_r, f_y, \theta_i) = \frac{N}{\theta f_r} \times S_{12}(f_r, f_y, \theta_i) \times H_{ST}^2(f_z). \tag{19}$$

where $N / (\theta \times f_r)$ is the spoke density and $f_z = f_r \times \sin(\theta_i)$. Then the calculated Ψ_{13} and S_{13} should be mapped from the (f_r, f_y, θ_i) to the (f_x, f_y, f_z) coordinates:

$$\begin{cases} \psi_{13}(f_x, f_y, f_z) = \psi_{13}(f_r, f_y, \theta_i) \\ S_{13}(f_x, f_y, f_z) = S_{13}(f_r, f_y, \theta_i) \end{cases}, \text{ where } \begin{cases} f_x = f_r \cos(\theta_i) \\ f_z = f_r \sin(\theta_i) \end{cases} \tag{20}$$

Stage 14: 3D sampling of the voxel matrix. The final stage describes the 3D sampling and NPS aliasing effect associated with the reconstructed voxel dimensions of $d_x = d_y = 50$ µm and $d_z = 1$ mm. Considering a typical tomographic reconstructed slice at 4 cm above detector, this should lead to an insignificant geometric magnification $M = (1 + d_2/d_1) = 1 + 4/65 = 1.07$. Since the spatial frequency axes are not scaled down by this magnification value (≈ 1), the geometric magnification should not greatly affect the spatial resolution. In this study, the magnification factor was ignored. The aliased 3D NPS is given by (Zhao and Zhao 2008b, Tward and Siewerdsen 2008, Gang *et al* 2011)

$$\begin{aligned} S_{14}(f_x, f_y, f_z) &= S_{13}(f_x, f_y, f_z) *** \text{III}(f_x, f_y, f_z) \\ &= \sum_{i,j,k} S_{14}(f_x, f_y, f_z)\delta\left(f_x - \frac{i}{d_x}, f_y - \frac{j}{d_y}, f_z - \frac{k}{d_z}\right), \end{aligned} \tag{21}$$

where i, j and k are integers and III(f_x, f_y, f_z) is a 3D sampling function. Since the slice thickness filter was applied to the reconstruction, the impact of z-direction NPS aliasing is eliminated in this study. The signal spectrum does not change during this process, $\Psi_{14}(f_x, f_y, f_z) = \Psi_{13}(f_x, f_y, f_z)$.

The 3D MTF and normalized NPS (NNPS) and DQE are given by

$$MTF(f_x, f_y, f_z) = \text{Norm}\left[\psi_{14}(f_x, f_y, f_z)\right], \tag{22}$$

$$NNPS(f_x, f_y, f_z) = S_{14}(f_x, f_y, f_z), \tag{23}$$

$$DQE(f_x, f_y, f_z) = \frac{\theta f_r}{N\overline{\overline{q}}_0} \cdot \frac{\psi_{14}^2(f_x, f_y, f_z)}{S_{14}(f_x, f_y, f_z)}, \tag{24}$$

where the Ψ_{14} is normalized to unity as the 3D MTF and the term $\theta f_r/N$ is used to normalize the spoke density for the 3D DQE calculation (Tward and Siewerdsen 2008). In this study, the 3D MTF, NNPS and DQE are used as evaluation metrics for detector 3D imaging performance. We recognize that the 3D DQE can be affected by filters during reconstruction. However, the study of the reconstruction filters' impact on the 3D imaging characteristics is outside the scope of this paper.

For DBT, one slice of the reconstructed tomographic image contains information of f_z ranging from $-f_{z,\mathrm{Nyq}}$ to $+f_{z,\mathrm{Nyq}}$. Therefore, we evaluate the in-plane MTF, NNPS and DQE by integrating the 3D parameters over f_z (Zhao and Zhao 2008b)

$$MTF_{ip}(f_x, f_y) = \mathrm{Norm}\left[\int_{-f_{z,Nyq}}^{+f_{z,Nyq}} MTF(f_x, f_y, f_z)df_z\right], \quad (25)$$

$$NNPS_{ip}(f_x, f_y) = \int_{-f_{z,Nyq}}^{+f_{z,Nyq}} NNPS(f_x, f_y, f_z)df_z, \quad (26)$$

$$DQE_{ip}(f_x, f_y) = d_z\int_{-f_{z,Nyq}}^{+f_{z,Nyq}} DQE(f_x, f_y, f_z)df_z, \quad (27)$$

where the d_z (= 1 mm) term is used to normalize the in-plane DQE as $d_z = 1/(2f_{z,\mathrm{Nyq}})$. The in-plane DQE is considered as an average of the 3D DQE over f_z. The integrated 2D in-plane MTF, NNPS and DQE are used to evaluate the CMOS APS detector 3D imaging performance for DBT.

3. Results and Discussion

3.1. Angle-dependent 2D imaging performance of the DynAMITe detector

The 2D MTF, NNPS and DQE parameters for the 50 μm pixel pitch DynAMITe CMOS APS detector at oblique incident angles ranging from 0 to 30° are measured. Both the horizontal (parallel to the rotary plane) and vertical (parallel to the rotary axis) MTF parameters were extracted. In Figure 3, it is observed that beam obliquity only blurs the horizontal MTF (x or u direction in this study). The vertical MTF is not affected by oblique projection angles (x-ray source moving on the horizontal direction).

Figure 4(a) shows the horizontal MTF component associated with the beam obliquity, i.e., $\mathrm{MTF}_{\mathrm{ob}}(u,\theta_{\mathrm{i}})$, extracted from measured MTF data by equation (2) and cascaded system analysis by equation (7). A scintillator thickness t of 150 μm was used in the calculation, which agrees with the scintillator thickness used in the prototype CMOS APS detector. The result demonstrates that a wide x-ray projection angle (e.g. $\theta_{\mathrm{i}} > 20°$) will reduce the MTF by more than 40% especially at high spatial frequencies greater than 5 mm^{-1}. Therefore, for a 50 μm pixel pitch CMOS APS detector with a Nyquist frequency of 10 mm^{-1}, it is necessary to characterize the 2D angle-dependent detector response and include it in the 3D cascaded system analysis.

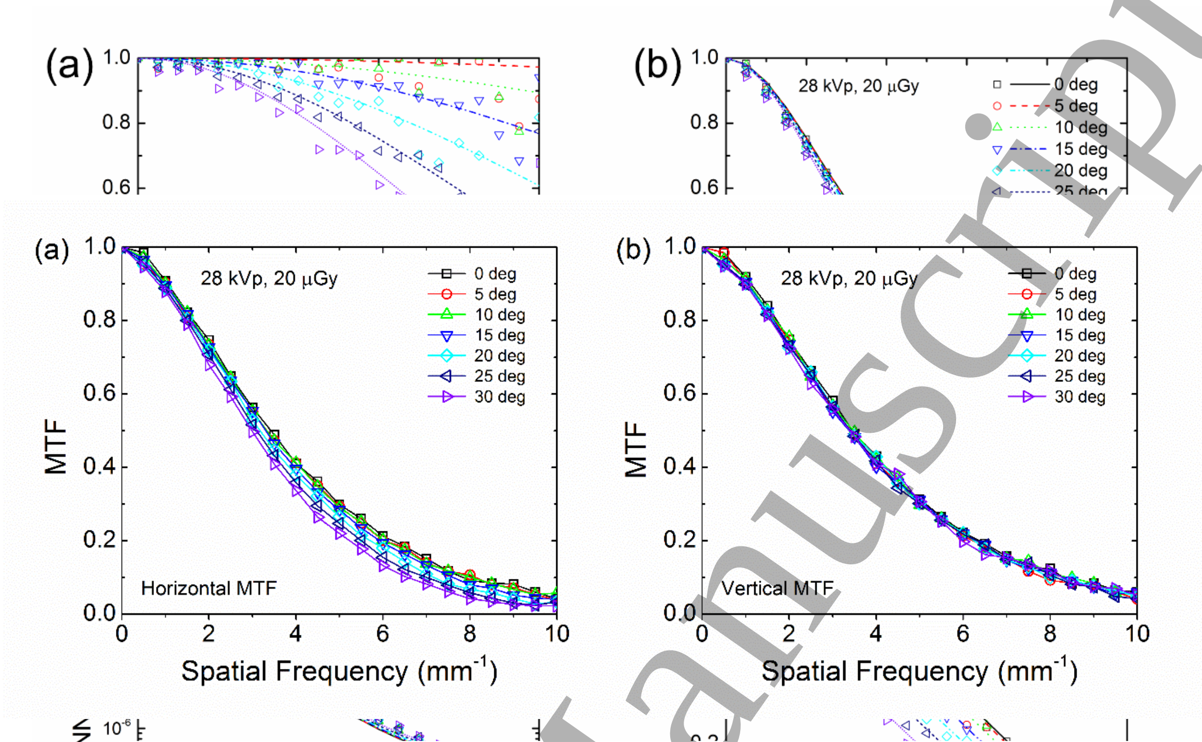

Figure 3. Experimental (a) horizontal (x-direction) and (b) vertical (y-direction) MTF parameter at x-ray projection angles ranging from 0 to 30 degrees. Simulation results are not shown in this figure.

Spatial Frequency (mm^{-1}) Spatial Frequency (mm^{-1})

Figure 4. Experimental (symbols) and simulated (lines) horizontal x-direction (a) MTF associated with the oblique incident angles, (b) detector MTF, (c) NNPS and (d) DQE parameters at incident beam angles θ_i ranging from 0 to 30 degrees.

As shown in Figure 4(b), since MTF(u,θ_i) = MTF$_{ob}$(u,θ_i) × MTF(u,0), the detector spatial resolution, MTF(u,θ_i), is degraded by the beam obliquity. On the other hand, both the experimental and simulation results (Figure 4(c)) indicate that the NNPS(u,θ_i) is not greatly influenced by θ_i. As a result, based on equation (4), the angle-dependent DQE(u,θ_i) at high spatial frequency range is degraded by the MTF^2(u,θ_i). Also we expect that DQE(u,θ_i) at zero spatial frequency, i.e., DQE(0,θ_i), will be reduced by a factor of cos(θ_i) due to the reduction of x-ray fluence at θ_i. The modeled angle-dependent 2D MTF and NNPS data were used as the input at stage 11 for the 3D cascaded system analysis.

Previously, the 2D angle-invariant cascaded system analysis model was validated for the DynAMITe detector (Zhao *et al* 2015b). Specifically, the gain stages and detector nonlinearity were verfied through mean signal and variance measurements and simulations; the zero-degree MTF, NNPS and DQE at various air kerma values were also validated.

Before implementation of cascaded system analysis to the 3D spatial frequency domain, it is critical to verfiy the 2D angle-dependent model. The maximum absolute errors (Δx = |x$_{sim}$ − x$_{exp}$|) between the simulated and experimental MTF and DQE values (within entire spatial frequency range for all projection angles) are 0.04 and 0.05 (mean absolute errors are 0.011 and 0.015 for MTF and

DQE), respectively. The maximum absolute errors occur at low spatial frequencies (<1 mm^{-1}). This is mainly due to the non-ideal MTF Lorentz fitting (stage 3) at low frequencies. We believe that the absolute errors are small and should not affect the results presented in this paper.

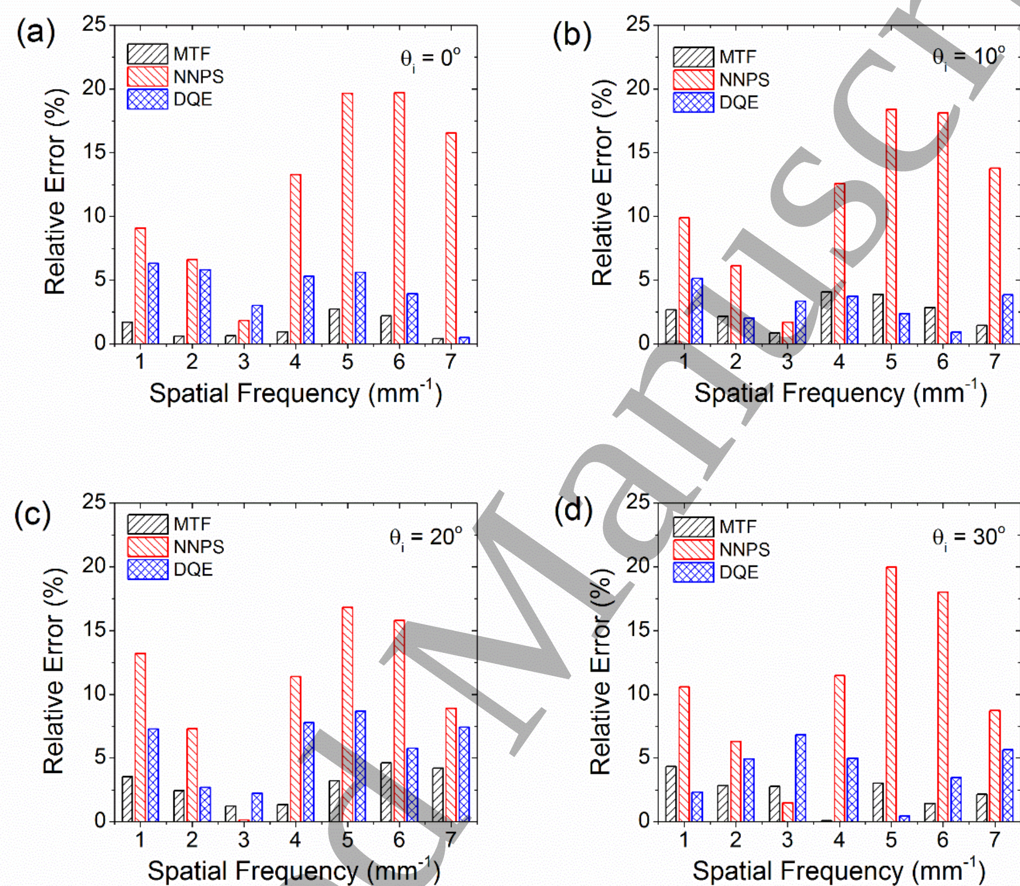

Figure 5. Relative errors (%) between simulated and measured MTF, NNPS and DQE parameters at x-ray beam projection angles of (a) 0°, (b) 10°, (c) 20° and (d) 30°. Spatial frequencies from 1 to 7 mm^{-1} are chosen.

The relative errors ($\sigma_{error} = |x_{sim} - x_{exp}| / x_{sim}$) between the experimental and simulated MTF, NNPS and DQE results at x-ray projection angles of 0, 10, 20 and 30 degrees are shown in Figure 5. At higher spatial frequencies (8 – 10 mm^{-1}), due to the very small MTF values, a negligible absolute error (e.g. 0.01) will lead to a large relative error. Hence, spatial frequencies greater than 8 mm^{-1} (corresponding to MTF smaller than 0.1) are omitted in Figure 5. The relative error of the MTF parameter is <4.6%. The NNPS parameter shows a relative error of <20%. In the cascaded system analysis, NNPS was calculated by multiplication of the square of several transfer functions ($T^2(u,v)$). Thus, the errors in MTF simulation is accumulated and amplified as the NNPS error. The NNPS deviation trend for cascaded system analysis was also observed in other studies (El-Mohri *et al* 2007, Vedantham *et al* 2004). Since the MTF and NNPS errors in the cascaded system analysis are correlated, the DQE error can be reduced (proportional to MTF^2/NNPS). The relative errors of the

DQE parameter are <8.7% under various angles and spatial frequencies. The DQE errors are within the accepted precision (10%) based on the IEC standard (IEC 62220-1-2: 2007). Hence, the angle-dependent cascaded system analysis demonstrates acceptable agreement with the experimental results. The verified angle-dependent 2D cascaded system analysis will be used as the input for the 3D cascaded system analysis.

3.2. Three-dimensional imaging performance of the DynAMITe detector

As described in section 2.2, the 3D MTF, NNPS and DQE in the (f_x, f_y, f_z) space was calculated in combination with the FBP reconstruction. A typical DBT x-ray tube voltage of 28 kVp was used. The detector air kerma (DAK) was 8.57 μGy to realize a mean glandular dose (MGD) of 1.5 mGy. If a 4.5 cm breast tissue with 50% glandularity is considered, this will lead to an entrance surface air kerma (ESAK) of 0.24 mGy and a MGD of 1.5 mGy for 21 projection views. The MGD calculation was described previously elsewhere (Zhao *et al* 2015a, 2015b). The impact of focal spot size is not currently included, but it will be discussed in section 3.5.

Figure 6 shows the simulated 3D MTF, NNPS and DQE in the (a) x-y plane (f_x, f_y), while f_z = 0 and (b) x-z plane (f_x, f_z), while f_y = 0. Although these 3D parameters have not been empirically measured in this study, the adopted 3D cascaded system analysis model based on FBP reconstruction

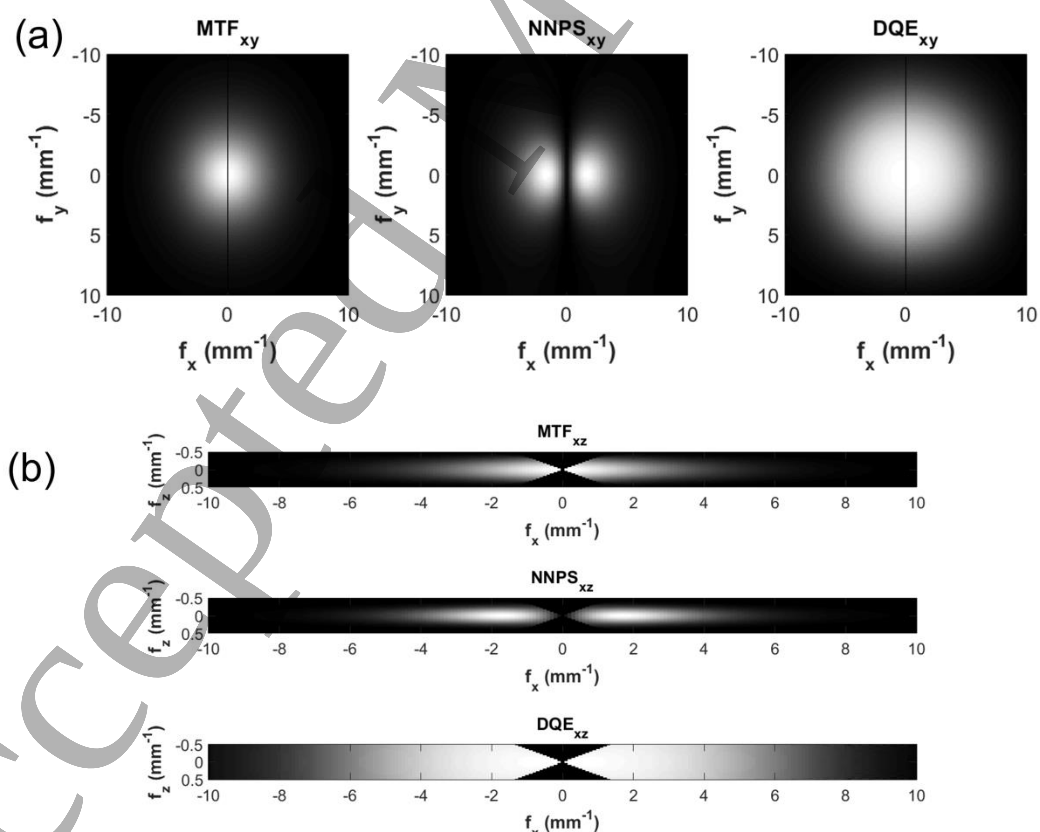

Figure 6. Calculated 3D MTF, NNPS and DQE in the (a) x-y plane: (f_x, f_y), while f_z = 0 and (b) x-z plane: (f_x, f_z), while f_y = 0. The 3D MTF, NNPS and DQE were calculated using Eq. (22), (23) and (24), respectively.

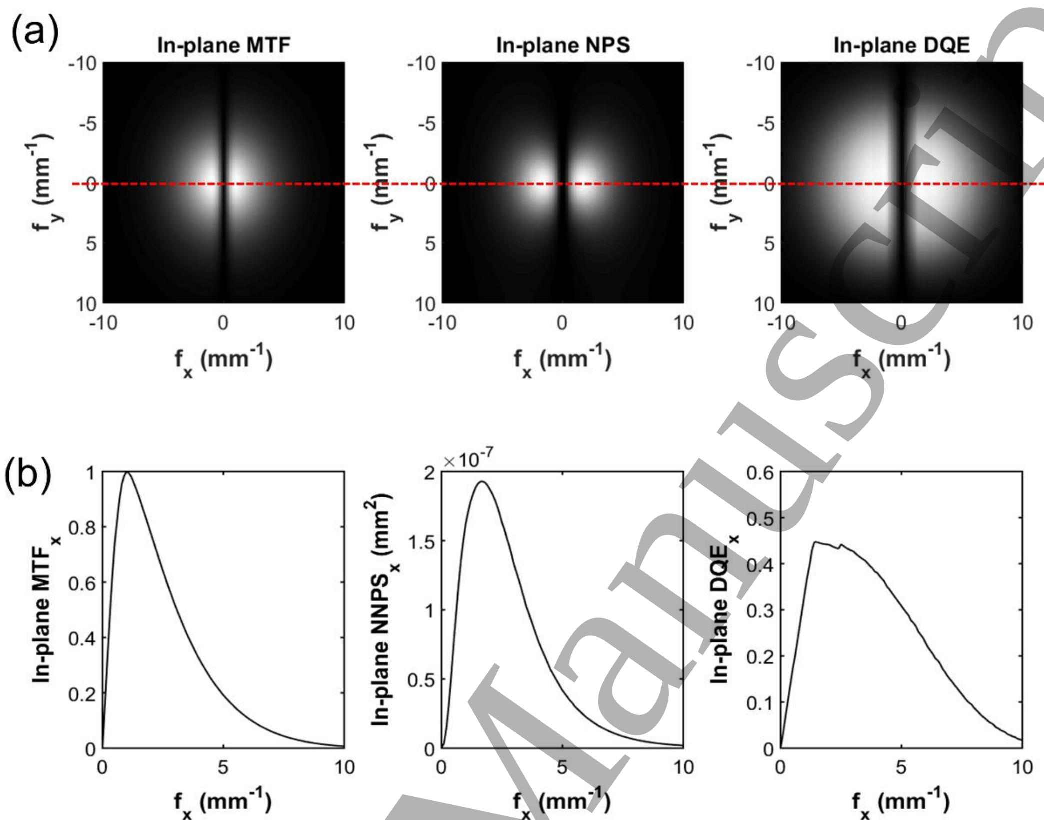

Figure 7. (a) In-plane MTF, NNPS and DQE calculated by integrating 3D MTF, NNPS and DQE over f_z. (b) In-plane MTF, NNPS and DQE for x direction (f_y = 0).

method have been validated previously by others with a good agreement between calculated and experimental results (Zhao *et al* 2009). Therefore, the 3D MTF, NNPS and DQE presented in this work should be reliable. The obtained result demonstrates that a high spatial resolution of around 8 mm^{-1} in the x-y plane can be achieved. The black line observed in the middle (f_x = 0) of the x-y plane MTF and DQE is due to the ramp filter (H_{RA}) reaching zero at f_x = 0. The x-z plane MTF, NNPS and DQE vanishes at low spatial frequencies with angles greater than the maximum projection angle. This is associated with the acquisition geometry (limited projection angle range) of DBT and will lead to poor image quality at low spatial frequencies. The impact of projection angle range on the 3D imaging performance will be discussed in section 3.3.

Figure 7(a) shows the calculated in-plane MTF(f_x, f_y), NNPS(f_x, f_y) and DQE(f_x, f_y) by integrating the 3D MTF, NNPS and DQE over f_z (equation (25-27)). The in-plane MTF, NNPS and DQE are considered as the figure of merits to characterize the 3D detector performance for DBT. The horizontal in-plane MTF, NNPS and DQE (Figure 7(b)) are extracted from Figure 7(a) by taking f_y = 0. In the following sections, only the in-plane MTF, NNPS and DQE are shown (to simplify the complexity of the presented figures) as the figure of merits to describe the 3D imaging performance of the DynAMITe CMOS APS detector.

Although the 2D detector MTF and DQE is degraded by the oblique incident angles at high spatial frequencies, it does not affect the 3D imaging performance significantly. This is because f_z is limited within a narrow range from -0.5 to 0.5 mm^{-1}. As a result, as shown in Figure 6(b), the impact of wide angle, high frequency regions are eliminated. The maximum in-plane DQE achieved by the DynAMITe CMOS APS detector is close to 0.5; this value is mainly limited by the scintillator absorption ($\overline{g_1}(\theta_i = 0)$ that is around 0.56). The maximum in-plane DQE is comparable to the 2D DQE of the Siemens MAMMOMAT a-Se direct conversion DBT system (Zhao and Zhao 2008a). To improve the in-plane DQE, a thicker scintillator could be considered. However, such thicker scintillator could increase the scintillator blurring effect and affect the image resolution. Another possible solution will be proposed in section 3.6. It is also shown that the horizontal in-plane DQE is proportional to f_x in the low spatial frequency region (< 2 mm^{-1}), which is associated with the limited projection angle range for DBT.

3.3. *Impact of the projection angle range*

The impact of projection angle range (from ±15° to ±30°) on 3D MTF, NNPS and DQE are evaluated. The 28 kVp tube voltage, 21 projection views and 1.5 mGy MGD are kept constant. Based on the simulation results (not shown), a wider blank gap (e.g. Figure 7(a)) appears in the middle of the in-plane MTF, NNPS and DQE and a wider "triangular" blank region (e.g. Figure 6(b)) can be observed at low f_x values of the x-z plane MTF, NNPS and DQE, if a narrower projection angle range (e.g. ±15°) is used. The blank regions indicate loss of image information in the low spatial frequency region, which can be associated with large, low contrast mass detection in DBT (Zhao *et al* 2009). As shown in Figure 8, increase of the projection angle range will shift the peak of in-plane MTF to lower frequencies and improve the in-plane DQE at low frequency region. This is consistent with the experimental and cascaded system modeling results reported by Zhao *et al* (2009). Based on our simulation results, we can confirm that a wider DBT projection angle range will result in better

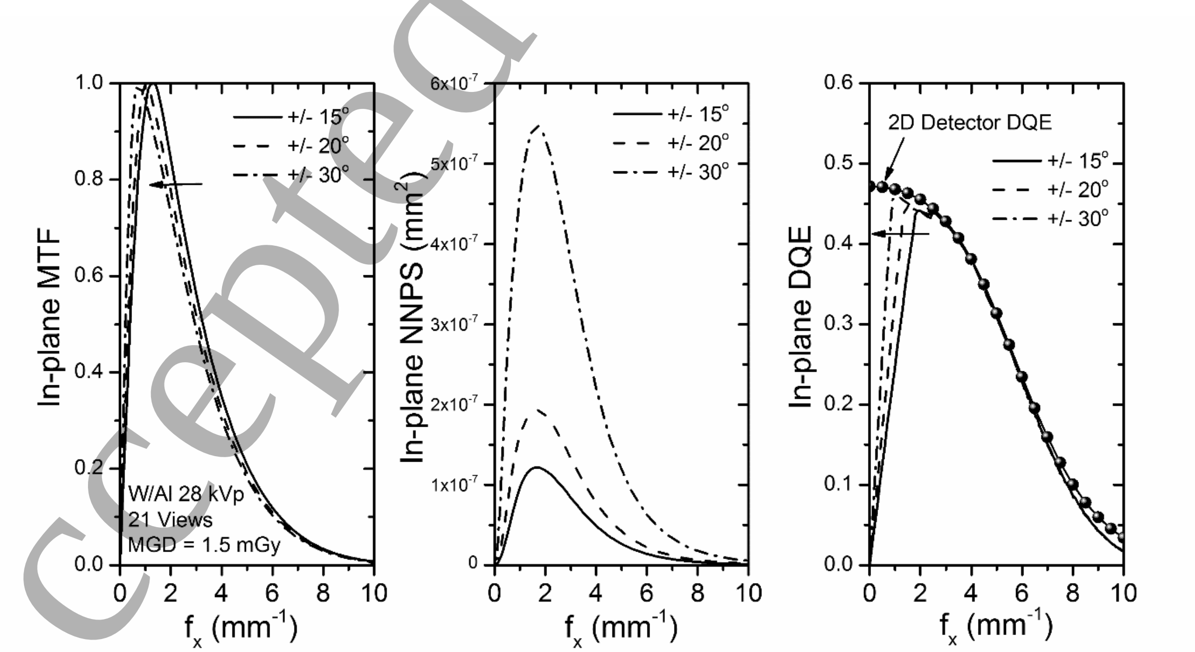

Figure 8. Horizontal x-direction in-plane (a) MTF, (b) NNPS and (c) DQE for projection angle range of ±15°, ±20° and ±30° at MGD of 1.5 mGy.

detection of low contrast objects such as masses (Zhao *et al* 2009, Goodsitt *et al* 2014). However, more projection views will result in a higher MGD, which is not desirable from the patient point-of-view. A possible solution to address this problem would be to have non-uniform dose distribution at different projection angles. It was also reported that a modified ramp filter with a non-zero flat transfer function (H_{RA}) at low frequencies can be used to improve the low-frequency reconstructed image quality (Zhou *et al* 2007). The evaluation of the reconstruction filters impact is not considered in this study. In the following sections, the projection angle range is fixed at ±20° for consistency.

Also shown in Figure 8, the in-plane DQE at high spatial frequency region almost overlaps the 2D detector DQE. Therefore, it is demonstrated that the projection angle range and the FBP image reconstruction method will not affect the 3D imaging performance of a CMOS APS detector at high spatial frequencies, which is desirable for subtle microcalcification detection. Hence we can conclude that to detect small features (around 100 μm in size) such as microcalcifications, the DBT detector requires to have both a high resolution and low noise characteristics. This can be realized, for example, using the CMOS or amorphous oxide TFT-based APS technology (Zhao and Kanicki 2014, Zhang *et al* 2013, Cheng *et al* 2016).

3.4. Impact of mean glandular dose

The current MGD used for DBT is around 1.5 mGy for an average breast with 50% glandularity (Sechopoulos *et al* 2007, Feng and Sechopoulos 2012, Sechopoulos *et al* 2014). In this study, the impact of dose on the 3D imaging performance is evaluated by varying the calculated MGD values from 0.5 to 1.5 mGy (Figure 9). As expected, dose does not change the in-plane MTF, but is inversely proportional to the normalized NPS. It can be observed that the in-plane DQE only decreases slightly, by about 5 and 15% averaged over the entire spatial frequency range, if MGD is reduced from 1.5

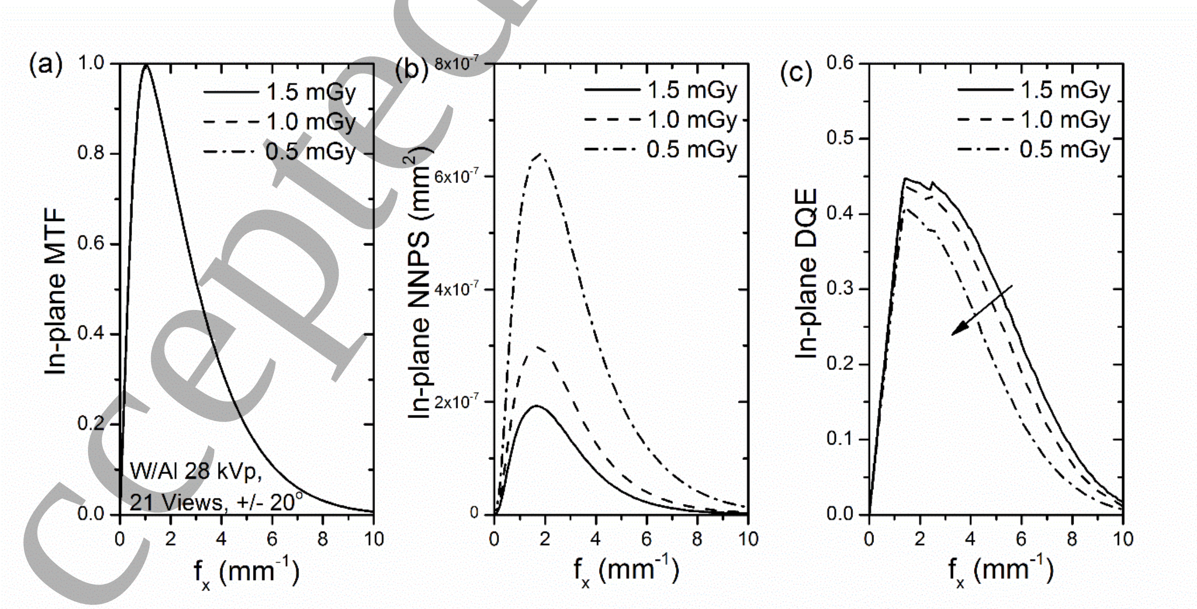

Figure 9. Horizontal x-direction in-plane (a) MTF, (b) NNPS and (c) DQE for MGD ranging from 0.5 – 1.5 mGy at the projection angle range of ±20.

mGy to 1.0 and 0.5 mGy, respectively. This result indicates that the 3D imaging performance of the detector under investigation does not decrease significantly at very low dose. Therefore, possible dose reduction could be achieved using the 50 µm pixel pitch CMOS APS x-ray detector, because the low electronic noise of this detectors (σ_R ~ 150 e^-) is not the dominant noise component at low dose exposures. The noise at low doses (i.e., 0.5 – 1.5 mGy) is quantum noise limited. Under this condition, we expect the image quality to be approximately proportional to the square root of the x-ray fluence (i.e. dose). On the other hand, if the electronic noise is high (e.g., a-Si:H TFT PPS detectors with σ_R > 1000 e^-), the imager noise at low exposure is dominated by the electronic noise floor. As a result, image signal-to-noise ratio (SNR) decreases rapidly, if a very low dose is used. Hence, a high resolution CMOS APS detector is a very promising technology for next generation low dose DBT system.

3.5. Impact of focal spot size

In DBT, the impact of focal spot blurring effect should be considered. Figure 10 shows a comparison between the calculated in-plane and x-z plane MTF, NNPS and DQE (a) without focal spot size blurring and (b) with a source focal spot size (a_{fs} in equation (9)) of 3 mm. As described in equation (8), a large a_{fs} will lead to a large effective focal spot size on the detector (a_f) that blurs the MTF

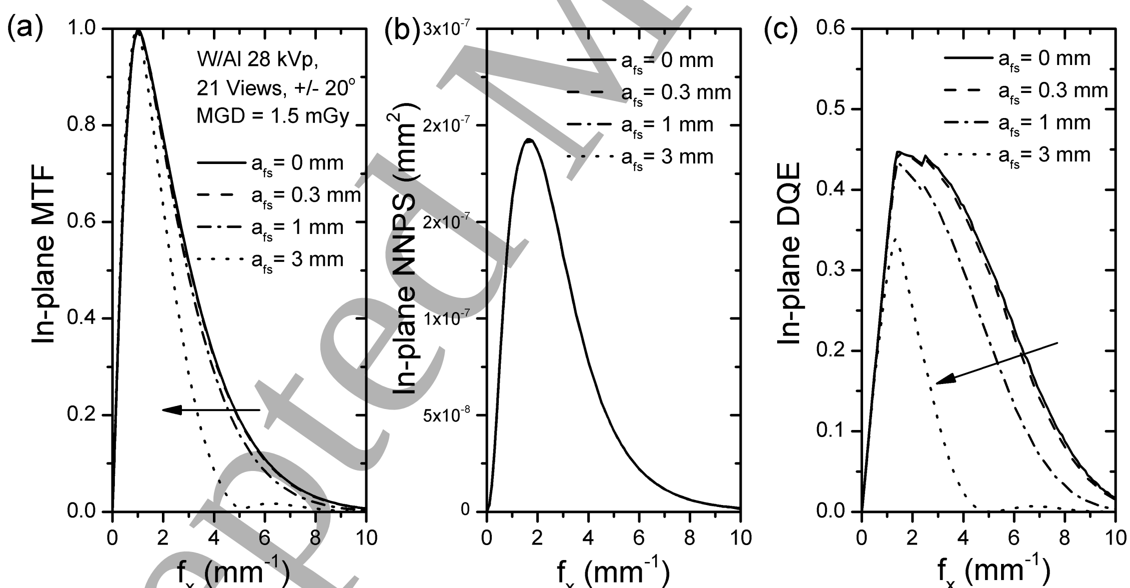

Figure 10. Horizontal x-direction in-plane (a) MTF, (b) NNPS and (c) DQE for focal spot size ranging from 0 to 3 mm at the projection angle range of ±20° and MGD of 1.5 mGy.

laterally. On the other hand, as shown in Figure 10 (b), the focal spot size will not affect the NNPS. Hence, the in-plane DQE is dramatically decreased by the square of MTF over the entire spatial frequency range, if a_{fs} is greater than 1 mm. To maintain a good image quality, an x-ray tube focal spot size of 0.3 mm or smaller should be used. This conclusion is consistent with the DBT industry practice using a focal spot size of 0.3 mm (Ren *et al* 2005).

Another type of focal spot blurring is due to the focal spot motion during an x-ray pulse. This

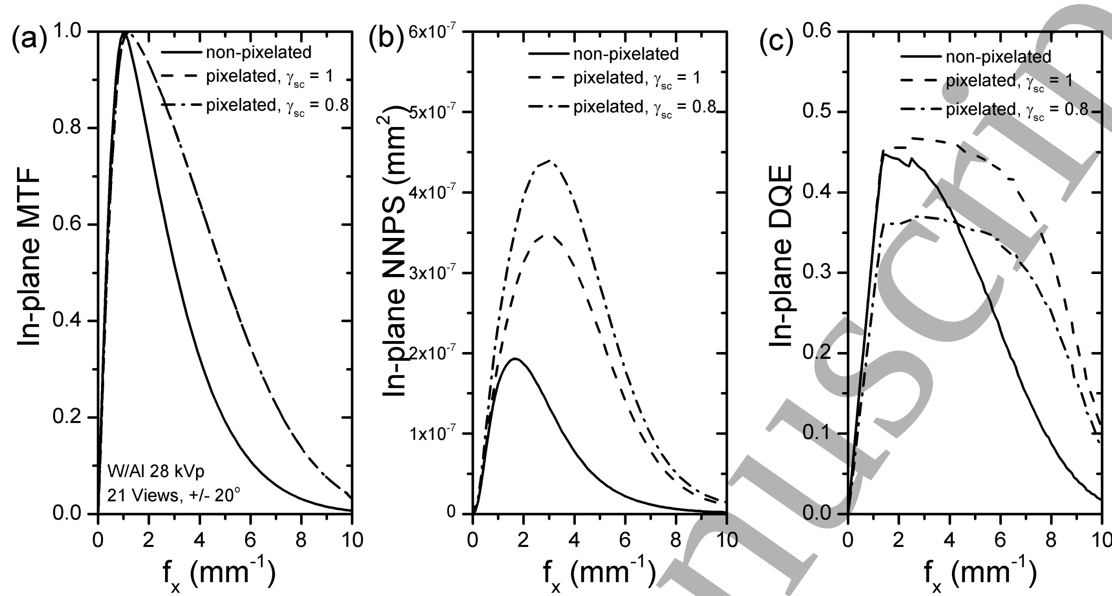

Figure 11. Horizontal x-direction in-plane (a) MTF, (b) NNPS and (c) DQE for standard non-pixelated scintillator and 50 µm pixelated scintillators with a fill factor of unity and 0.8. The projection angle range is ±20° and the MGD is 1.5 mGy.

effect, evaluated by Zhao and Zhao (2008), shows reduction in DQE on the f_x direction. In this study, the focal spot motion blurring effect is eliminated by using the standard step-and-shoot x-ray tube motion. It was reported that such tube motion provides better visibility of microcalcifications due to the improved MTF at high spatial frequencies (Shaheen *et al* 2011).

3.6. Impact of pixelated scintillator

The maximum in-plane DQE achieved using the DynAMITe detector in combination with the 150 µm CsI:Tl scintillator is around 0.5. It is well-known that the maximum DQE is associated with the scintillator thickness. In general, a thicker scintillator can improve the quantum detection efficiency and thus the zero-frequency DQE. On the other hand, the MTF at high spatial frequencies would be degraded due to the optical signal cross-talk between adjacent pixels (Zhao *et al* 2004). The ideal scintillator should achieve both a high x-ray absorption with minimum blurring.

To prevent the scintillator optical blurring, pixelated scintillators have been proposed and evaluated (Nagarkar *et al* 2003, Miller *et al* 2005, Kim *et al* 2008a, Cha *et al* 2006). Pixelated scintillators can be fabricated by (a) patterning a pre-deposited CsI:Tl film (Nagarkar *et al* 2003), (b) thermal evaporation CsI:Tl on a pre-patterned pixelated substrate (Cha *et al* 2008, 2009) or (c) filling scintillating phosphors in pixelated molds (2D wells) (Simon *et al* 2008). It has been reported by different groups that pixelated scintillators improve the MTF and DQE at high spatial frequencies (Cha *et al* 2009, Kim *et al* 2008b, Cha *et al* 2008, 2006, Simon *et al* 2008, Nagarkar *et al* 2003). In this work, the impact of scintillator pixelation on the 3D imaging performance is evaluted.

In the 3D cascaded system analysis for non-pixelated scintillator having thickness of 150 µm, a Loreantz fit was used to simulate the 2D transfer function associated with scintillator blurring effect

($T_3(u, v)$). To described the signal transfer of pixelated scintillator, $T_3(u, v)$ is modified as $T_3(u, v) = \mathrm{sinc}(a_{sc} \cdot u) \times \mathrm{sinc}(a_{sc} \cdot v)$, where a_{sc} is the scintillator pixel pitch (Kim *et al* 2008b). It should be noted that we assume that the optical cross-talk between adjacent pixels is completely removed (ideal case) by the scintillator pixelation. This could be realized by using the 2D mold or fill the gap with reflective oxides (Nagarkar *et al* 2003, Miller *et al* 2005, Simon *et al* 2008). In addition, a scintillator performance correction factor (γ_{sc}) is multiplied by the scintillator absorption ($\bar{g}_1$); γ_{sc} may include the combined impacts of scintillator fill factor (defined by the active scintillator area over the entire scintillator pixel area) and/or the reduction in scintillator absorpition. In this study, we consider a scintillator pixel pitch $a_{sc} = a_{pix} = 50$ μm and a γ_{sc} in the range of 0.8 to 1.

Figure 11 shows the in-plane and x-z plane MTF, NNPS and DQE for the 50 μm pixel pitch DynAMITe CMOS APS detector with (a) a standard non-pixelated scintillator as the reference and (b) a 150 μm thick pixelated scintillator having $a_{sc} = 50$ μm and $\gamma_{sc} = 1$. It is obvious that the 3D MTF, NNPS and DQE expand over both f_x and f_y directions. As shown in Figure 11, the in-plane MTF and DQE of detector with the pixelated scintillator improves significantly (by more than 0.2) in the high spatial frequency range ($f_x > 5$ mm^{-1}). Therefore, the spatial resolution of the reconstructed images is expected to be improved, which is a promising feature for small microcalcification (~100 μm) detection. On the other hand, a limited γ_{sc} will reduce the in-plane DQE. Thereby, it is critical that the scintillator has a high fill factor and x-ray absorption to maintain a high DQE. Hence, using a thicker pixelated scintillator would be desirable, since no degradation in spatial resolution is expected in such case. From the cascaded system model, it is indicated that a 250 μm thick scintillator can increase the scintillator x-ray absorption by 18% ($\bar{g}_1 \sim 0.66$) in comparison to the 150 μm thick scintillator. We believe that the pixelated scintillator in combination with the high-resolution, low-noise CMOS APS detector should be suitable for microcalcifications detection with size ranging from 100 to 150 μm. Also a DBT system based on the CMOS APS detector will allow radiologists to better visualize the shape of microcalcifications with the image information contained in the high spatial frequency range for observer studies. Another suggested approach to improve the spatial resolution is to use the direct conversion amorphous selenium (a-Se) photodetector in combination with the CMOS APS backplane (Scott *et al* 2014, Parsafar *et al* 2015).

3.7. 3D imaging performance comparison of CMOS APS and indirect a-Si:H TFT PPS detectors

Up to date, currently available DBT systems on the market are all based on the direct or indirect a-Si:H TFT PPS technology (Sechopoulos 2013b, NHS 2015). Therefore, it is important to compare the 3D imaging performance of the CMOS APS detector with the a-Si:H TFT-based PPS detectors. The 2D and 3D MTF, NPS and DQE for a direct a-Se/a-Si:H TFT PPS system (Siemens system) has already been intensively characterized and reported (Zhao *et al* 2009, Zhao and Zhao 2008b, Zhou *et al* 2007, Zhao and Zhao 2008a, Hu *et al* 2008). In comparison to the direct a-Se/a-Si:H TFT PPS system, the DynAMITe CMOS APS detector demonstrates similar 3D imaging performance at low spatial frequency region, but can significantly extend the x-y plane spatial resolution from 5.88 (85 μm pixel pitch) to 10 mm^{-1}. In this section, we discuss the detector performance of the DynAMITe CMOS APS and CsI:Tl/a-Si:H TFT PPS technologies by making the parameter changes in the 3D cascaded system model shown in Table 1.

Table 1. Simulation parameters used for the DynAMITe CMOS APS and CsI:Tl/a-Si:H TFT PPS systems.

	DynAMITe SP detector	CsI:Tl/a-Si:H TFT PPS
Pixel pitch (µm)	50	100
Scintillator thickness (µm)	150	250
Optical coupling efficiency	0.4	0.4 and 0.8
Conversion gain	0.02 DN/e^-	–
Electronic noise (e^-)	150	1500

In general, the indirect PPS detector has a larger pixel pitch (around 100 µm). In the simulation, we consider a thicker CsI:Tl scintillator (250 µm) for the a-Si:H TFT PPS detector to improve the light output from the scintillator. The increased blurring associated with the thicker scintillator is ignored (ideal case). The impact of optical coupling efficiency of the CsI:Tl/detector interface is evaluated by increasing $\bar{g}_4$ from 0.4 to 0.8. The a-Si:H TFT PPS detector has a unity charge gain (in e^-/e^-) on the pixel level and suffers from a large electronic noise (~1500 e^-) dominated by the op-amp noise. All other parameters were not changed in the simulation.

Figure 12 shows the simulated in-plane MTF, NNPS and DQE parameters for the indirect CMOS APS and indirect a-Si:H TFT PPS detectors. In comparison to the DynAMITe CMOS APS detector, the indirect PPS detector shows a limited Nyquist frequency of 5 mm^{-1} and a high NNPS that is duplicated at f_x > 5 mm^{-1} due to a large pixel pitch (100 µm) and high electronic noise (1500 e$^-$), respectively. Thus, the in-plane DQE is lower in comparison to the DynAMITe detector in the entire spatial frequency range. Since the PPS does not have a conversion gain to boost the input signal (in e$^-$), the optical coupling efficiency of stage 4 needs to be optimized ($\bar{g}_4$ = 0.8) to achieve a higher in-plane DQE. It should be noted that the x-ray source and scintillator performance (e.g. quantum gain and light output) used for this simulation has not been optimized; this could lead to smaller calculated DQE in comparison to the product specification (~0.65) of GE SenoClaire system (Rh/Rh source at low dose DBT condition) (Souchay *et al* 2013). The simulated results for both PPS and APS detectors can be improved by i) scintillator performance enhancement and/or pixelation, ii) increasing the optical coupling efficiency, iii) noise reduction and iv) image reconstruction optimization.

As a future work, the developed 3D cascaded system analysis described above can be integrated with detectability index calculation by introducing various task functions (Gang *et al* 2011, Tward and Siewerdsen 2008, Hu and Zhao 2014, Siewerdsen and Jaffray 2000, Gang *et al* 2012, Richard *et al* 2005) to evaluate the detectability of objects of interest, such as small microcalcifications and low contrast masses.

4. Conclusion

The 2D MTF, NNPS and DQE parameters were measured and modeled at projection angles up to 30°

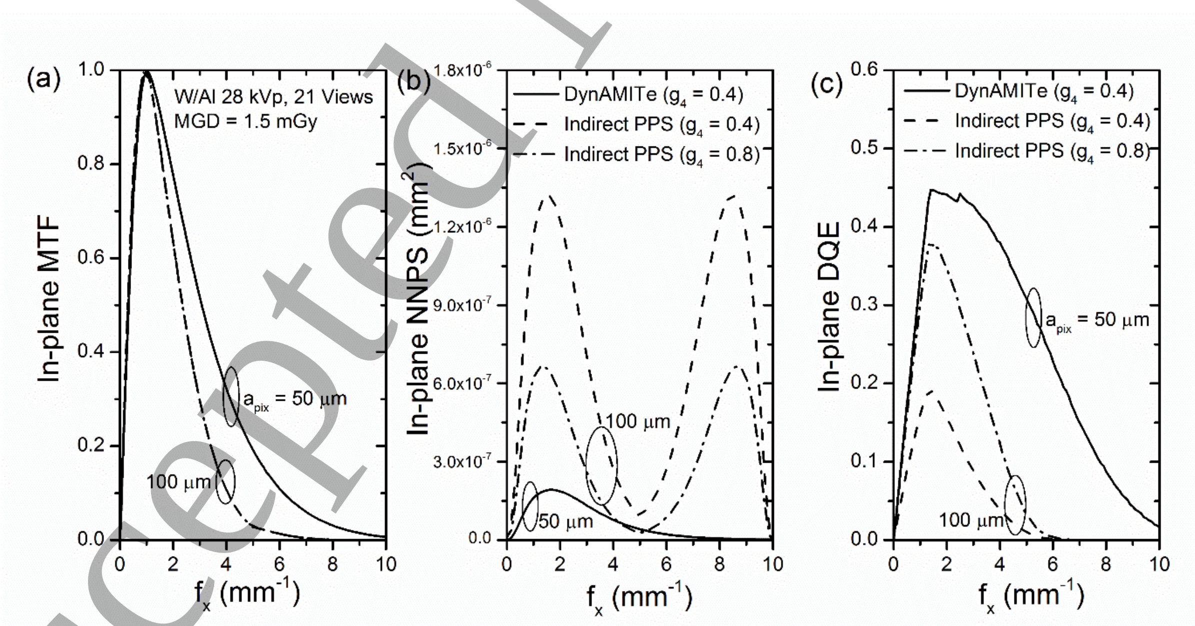

Figure 12. Horizontal x-direction in-plane (a) MTF, (b) NNPS and (c) DQE for the DynAMITe CMOS APS detector (150 µm CsI:Tl scintillator, 50 µm pixel pitch and 150 e$^-$ electronic noise) and a simulated indirect a-Si:H TFT PPS detector (250 µm CsI:Tl scintillator, 100 µm pixel pitch and 1500 e$^-$ electronic noise) at the projection angle range of ±20° and MGD = 1.5 mGy. The impact of optical coupling efficiency is also shown.

for the 50 μm pixel pitch, low-noise DynAMITe CMOS APS detector. The experimental and simulation results demonstrate that a wider incident projection angle will degrade the MTF and DQE in the high spatial frequency range, while the NNPS is not affected. A 3D cascaded system model in combination with the FBP reconstruction method was developed for the DynAMITe CMOS APS detector to evaluate its 3D imaging performance. Although the beam obliquity reduces the 2D detector MTF and DQE, it should not influence the reconstructed 3D image quality, if appropriate filters are applied using the FBP method. The impacts of acquisition geometry, dose and detector parameters were investigated using the 3D cascaded system analysis. It is shown that a wider projection angle range (e.g. 30°) will prevent image information loss at low spatial frequencies, which is suitable for large, low contrast objects (such as masses) detection. Low MGD (0.5 mGy) does not affect the CMOS APS detector response (in-plane DQE) due to the low electronic noise. We found that the dominant factors limiting the investigated CMOS APS detector 3D imaging performance include the focal spot size and the scintillator blurring effect. Specifically, a large focal spot size will remarkably decrease both the in-plane MTF, and DQE. To achieve satisfactory image quality for DBT, a focal spot size of smaller than 0.3 mm should be used. A remarkable improvement on the in-plane MTF and DQE are achieved when the pixelated scintillator is used to reduce its blurring effect. Although the scintillator pixel fill factor can reduce the x-ray photon capture and absorption when 50 μm pixel pitch is used, we believe that a thicker pixelated scintillator in combination with the CMOS APS detector can be used to address this issue. Finally, based on the simulation results, in comparison to a 100 μm pixel pitch indirect a-Si:H TFT PPS detector, the DynAMITe CMOS APS demonstrates improved in-plane MTF and DQE in the entire spatial frequency range.

Acknowledgements

The authors would like to acknowledge Dr. Bo Zhao from the University of Texas Southwestern Medical Center for the discussion of the 3D cascaded system analysis calculation. One of us (C. Zhao) would like to thank the EECS department, University of Michigan for the financial support.

References

Bohndiek S E, Blue A, Cabello J, Clark A T, Guerrini N, Evans P M, Harris E J, Konstantinidis A, Maneuski D, Osmond J, O'Shea V, Speller R D, Turchetta R, Wells K, Zin H and Allinson N M 2009 Characterization and Testing of LAS: A Prototype "Large Area Sensor" With Performance Characteristics Suitable for Medical Imaging Applications *Nucl. Sci. IEEE Trans.* **56** 2938–46

Cha B K, Bae J H, Kim B J, Jeon H and Cho G 2008 Performance studies of a monolithic scintillator-CMOS image sensor for X-ray application *Nucl. Instruments Methods Phys. Res. Sect. A Accel. Spectrometers, Detect. Assoc. Equip.* **591** 113–6

Cha B K, Bae J H, Lee C h., Jeon H, Kim H, Chang S, Kang B S and Cho G 2009 Improvement of the sensitivity and spatial resolution of pixelated CsI:Tl scintillator with reflective coating *Nucl. Instruments Methods Phys. Res. Sect. A Accel. Spectrometers, Detect. Assoc. Equip.* **607** 145–9

Cha B K, Kim B-J, Cho G, Jeon S C, Bae J H, Chi Y K, Lim G-H and Kim Y-H 2006 A Pixelated CsI (Tl) Scintillator for CMOS-based X-ray Image Sensor *2006 IEEE Nuclear Science Symposium Conference Record* (IEEE) pp 1139–43

Cheng M, Zhao C, Huang C and Kanicki J 2016 Amorphous InSnZnO Thin-Film Transistor Voltage-Mode Active Pixel Sensor Circuits for Indirect X-Ray Imagers 1–7

Choi J-G, Park H-S, Kim Y, Choi Y-W, Ham T-H and Kim H-J 2012 Characterization of prototype full-field breast tomosynthesis by using a CMOS array coupled with a columnar CsI(Tl) scintillator *J. Korean Phys. Soc.* **60** 521–6

El-Mohri Y, Antonuk L E, Zhao Q, Wang Y, Li Y, Du H and Sawant A 2007 Performance of a high fill factor, indirect detection prototype flat-panel imager for mammography *Med Phys* **34** 315–27

Esposito M, Anaxagoras T, Fant A, Wells K, Konstantinidis A, Osmond J P F, Evans P M, Speller R D and Allinson N M 2011 DynAMITe: a wafer scale sensor for biomedical applications *J. Instrum.* **6** C12064–C12064Esposito M, Anaxagoras T, Konstantinidis A C, Zheng Y, Speller R D, Evans P M, Allinson N M and Wells K 2014 Performance of a novel wafer scale CMOS active pixel sensor for bio-medical imaging. *Phys. Med. Biol.* **59** 3533–54

Feng S S J and Sechopoulos I 2012 Clinical Digital Breast Tomosynthesis System: Dosimetric Characterization *Radiology* **263** 35–42

Fujita H, Tsai D-Y, Itoh T, Doi K, Morishita J, Ueda K and Ohtsuka A 1992 A simple method for determining the modulation transfer function in digital radiography *IEEE Trans. Med. Imaging* **11** 34–9

Gang G J, Lee J, Stayman J W, Tward D J, Zbijewski W, Prince J L and Siewerdsen J H 2011 Analysis of Fourier-domain task-based detectability index in tomosynthesis and cone-beam CT in relation to human observer performance. *Med. Phys.* **38** 1754–68

Gang G J, Zbijewski W, Webster Stayman J and Siewerdsen J H 2012 Cascaded systems analysis of noise and detectability in dual-energy cone-beam CT *Med. Phys.* **39** 5145

Goodsitt M M, Chan H-P, Schmitz A, Zelakiewicz S, Telang S, Hadjiiski L, Watcharotone K, Helvie M a, Paramagul C, Neal C, Christodoulou E, Larson S C and Carson P L 2014 Digital breast tomosynthesis: studies of the effects of acquisition geometry on contrast-to-noise ratio and observer preference of low-contrast objects in breast phantom images. *Phys. Med. Biol.* **59** 5883–902

Hajdok G and Cunningham I A 2004 Penalty on the detective quantum efficiency from off-axis incident x rays *SPIE Med. Imaging* **5368** 109–18

Hejazi S and Trauernicht D P 1997 System considerations in CCD-based x-ray imaging for digital chest radiography and digital mammography. *Med. Phys.* **24** 287–97

Hu Y-H, Zhao B and Zhao W 2008 Image artifacts in digital breast tomosynthesis: investigation of the effects of system geometry and reconstruction parameters using a linear system approach. *Med. Phys.* **35** 5242–52

Hu Y-H and Zhao W 2014 The effect of amorphous selenium detector thickness on dual-energy digital breast imaging *Med. Phys.* **41** 111904

Hu Y-H and Zhao W 2011 The effect of angular dose distribution on the detection of microcalcifications in digital breast tomosynthesis. *Med. Phys.* **38** 2455–66

IEC 62220-1-2: 2007 *Medical Electrical Equipment: Characteristics of Digital X-ray Imaging Devices. Determination of the Detective Quantum Efficiency--Detectors Used in Mammography* (International Electrotechnical Commission)

Jain A, Bednarek D R, Ionita C and Rudin S 2011 A theoretical and experimental evaluation of the microangiographic fluoroscope: A high-resolution region-of-interest x-ray imager *Med. Phys.* **38** 4112

Jiang H, Kaercher J and Durst R 2016 Indirect-detection single-photon-counting x-ray detector for breast tomosynthesis *Proc. SPIE* vol 9783, ed D Kontos, T G Flohr and J Y Lo p 97833P

Kim H K, Cunningham I A, Yin Z and Cho G 2008a On the Development of Digital Radiography Detectors : A Review *Precis. Eng.* **9** 86–100

Kim H K, Yun S M, Ko J S, Cho G and Graeve T 2008b Cascade modeling of pixelated scintillator detectors for X-ray imaging *IEEE Trans. Nucl. Sci.* **55** 1357–66

Kim Y-S, Park H-S, Park S-J, Choi S, Lee H, Lee D, Choi Y-W and Kim H-J 2016 Characterizing X-ray detectors for prototype digital breast tomosynthesis systems *J. Instrum.* **11** P03022–P03022

Konstantinidis A, Anaxagoras T, Esposito M, Allinson N and Speller R 2012a DynAMITe: a prototype large area CMOS APS for breast cancer diagnosis using x-ray diffraction measurements *Proc. SPIE* vol 8313p 83135H

Konstantinidis A C, Olivo A and Speller R D 2011 Technical Note: modification of the standard gain correction algorithm to compensate for the number of used reference flat frames in detector performance studies. *Med. Phys.* **38** 6683–7

Konstantinidis A C, Szafraniec M B, Rigon L, Tromba G, Dreossi D, Sodini N, Liaparinos P F, Naday S, Gunn S, McArthur A, Speller R D and Olivo A 2013 X-ray performance evaluation of the dexela cmos aps x-ray detector using monochromatic synchrotron radiation in the mammographic energy range *IEEE Trans. Nucl. Sci.* **60** 3969–80

Konstantinidis A C, Szafraniec M B, Speller R D and Olivo A 2012b The Dexela 2923 CMOS X-ray detector: A flat panel detector based on CMOS active pixel sensors for medical imaging applications *Nucl. Instruments Methods Phys. Res. Sect. A Accel. Spectrometers, Detect. Assoc. Equip.* **689** 12–21

Mainprize J G, Bloomquist A K, Kempston M P and Yaffe M J 2006 Resolution at oblique incidence angles of a flat panel imager for breast tomosynthesis. *Med. Phys.* **33** 3159–64

Miller S R, Gaysinskiy V, Shestakova I and Nagarkar V V. 2005 Recent Advances in Columnar CsI(Tl) Scintillator Screens *Proc. SPIE* **5923** 59230F1-59230F10

Naday S, Bullard E F, Gunn S, Brodrick J E, O'Tuairisg E O, McArthur A, Amin H, Williams M B, Judy P G and Konstantinidis A 2010 Optimised Breast Tomosynthesis with a Novel CMOS Flat Panel Detector *Lecture Notes in Computer Science (including subseries Lecture Notes in Artificial Intelligence and Lecture Notes in Bioinformatics)* vol 6136 LNCS pp 428–35

Nagarkar V V., Tipnis S V., Gaysinskiy V B, Miller S R, Karellas A and Vedantham S 2003 New design of a structured CsI(Tl) screen for digital mammography *Medical Imaging 2003: Physics of Medical Imaging* vol 5030, ed M J Yaffe and L E Antonuk pp 541–6

NHS 2015 *Routine quality control tests for breast tomosynthesis (physicists) NHS Breast Screening*

Programme Equipment Report 1407

Park H S, Kim Y S, Kim H J, Choi Y W and Choi J G 2014 Optimization of configuration parameters in a newly developed digital breast tomosynthesis system *J. Radiat. Res.* **55** 589–99

Parsafar A, Scott C C, El-Falou A, Levine P M and Karim K S 2015 Direct-conversion CMOS X-ray imager with with 5.6 μm × 6.25 μm pixels *IEEE Electron Device Lett.* **36** 481–3

Patel T, Klanian K, Gong Z and Williams M B 2012 Detective Quantum Efficiency of a CsI-CMOS X-ray Detector for Breast Tomosynthesis Operating in High Dynamic Range and High Sensitivity Modes pp 80–7

Peters I M, Smit C, Miller J J and Lomako A 2016 High dynamic range CMOS-based mammography detector for FFDM and DBT *SPIE Medical Imaging. International Society for Optics and Photonics* vol 9783, ed D Kontos, T G Flohr and J Y Lo p 978316

Ren B, Ruth C, Stein J, Smith A, Shaw I and Jing Z 2005 Design and performance of the prototype full field breast tomosynthesis system with selenium based flat panel detector *Proc. SPIE Med. Imaging* **5745** 550–61

Richard S, Siewerdsen J H, Jaffray D A, Moseley D J and Bakhtiar B 2005 Generalized DQE analysis of dual-energy imaging using flat-panel detectors *Med Phys* **5745** 1397–413

Samei E, Flynn M J and Reimann D a 1998 A method for measuring the presampled MTF of digital radiographic systems using an edge test device. *Med. Phys.* **25** 102–13

Scott C C, Abbaszadeh S, Ghanbarzadeh S, Allan G, Farrier M, Cunningham I a. and Karim K S 2014 Amorphous selenium direct detection CMOS digital x-ray imager with 25 micron pixel pitch *Proc.SPIE Medical Imaging* vol 9033, ed B R Whiting and C Hoeschen p 90331G

Sechopoulos I 2013a A review of breast tomosynthesis. Part I. The image acquisition process. *Med. Phys.* **40** 14301

Sechopoulos I 2013b A review of breast tomosynthesis. Part II. Image reconstruction, processing and analysis, and advanced applications. *Med. Phys.* **40** 14302

Sechopoulos I, Sabol J M, Berglund J, Bolch W E, Brateman L, Christodoulou E, Flynn M, Geiser W, Goodsitt M, Jones a K, Lo J Y, Maidment A D a, Nishino K, Nosratieh A, Ren B, Segars W P and Von Tiedemann M 2014 Radiation dosimetry in digital breast tomosynthesis: report of AAPM Tomosynthesis Subcommittee Task Group 223. *Med. Phys.* **41** 91501

Sechopoulos I, Suryanarayanan S, Vedantham S, D'Orsi C and Karellas A 2007 Computation of the glandular radiation dose in digital tomosynthesis of the breast. *Med. Phys.* **34** 221–32

Shaheen E, Marshall N and Bosmans H 2011 Investigation of the effect of tube motion in breast tomosynthesis: continuous or step and shoot? *Proc. SPIE 7961; Med. Imaging 2011 Phys. Med. Imaging* **7961** 79611E

Siewerdsen J H, Antonuk L E, el-Mohri Y, Yorkston J, Huang W, Boudry J M, Cunningham I A, ElMohri Y, Yorkston J, Huang W, Boudry J M, Cunningham I A and el-Mohri Y 1997 Empirical and theoretical investigation of the noise performance of indirect detection, active matrix flat-panel imagers (AMFPIs) for diagnostic radiology *Med. Phys.* **24** 71–89

Siewerdsen J H and Jaffray D A 2000 Optimization of x-ray imaging geometry (with specific application to flat-panel cone-beam computed tomography) *Med. Phys.* **27** 1903

Siewerdsen J H and Jaffray D A 2003 Three-dimensional NEQ transfer characteristics of volume CT using direct- and indirect-detection flat-panel imagers *SPIE Med. Imaging 2003* **5030** 92–102

Simon M, Engel K J, Menser B, Badel X and Linnros J 2008 X-ray imaging performance of scintillator-filled silicon pore arrays *Med Phys* **35** 968–81

Souchay H, Carton K and Iordache R 2013 *SenoClaire White Paper* Online: http://www3.gehealthcare.com.br/~/media/Downloads/br/SenoClaire_Dose_White_Paper_-_DOC1403841.pdf

Tward D J and Siewerdsen J H 2008 Cascaded systems analysis of the 3D noise transfer characteristics of flat-panel cone-beam CT *Med. Phys.* **35** 5510

Vedantham S, Karellas A and Suryanarayanan S 2004 Solid-state fluoroscopic imager for high-resolution angiography: Parallel-cascaded linear systems analysis *Med. Phys.* **31** 1258–68

Zentai G 2011 Comparison of CMOS and a-Si flat panel imagers for X-ray imaging *2011 IEEE Int. Conf. Imaging Syst. Tech. IST 2011 - Proc.* 194–200

Zhang R, Bie L, Fung T C, Yu E K H, Zhao C and Kanicki J 2013 High performance amorphous metal-oxide semiconductors thin-film passive and active pixel sensors *Technical Digest - International Electron Devices Meeting, IEDM*

Zhao B and Zhao W 2008a Imaging performance of an amorphous selenium digital mammography detector in a breast tomosynthesis system. *Med. Phys.* **35** 1978–87

Zhao B and Zhao W 2008b Three-dimensional linear system analysis for breast tomosynthesis. *Med. Phys.* **35** 5219–32

Zhao B, Zhou J, Hu Y-H, Mertelmeier T, Ludwig J and Zhao W 2009 Experimental validation of a three-dimensional linear system model for breast tomosynthesis *Med. Phys.* **36** 240–51

Zhao C and Kanicki J 2014 Amorphous In-Ga-Zn-O thin-film transistor active pixel sensor x-ray imager for digital breast tomosynthesis. *Med. Phys.* **41** 91902

Zhao C, Kanicki J, Konstantinidis A C and Patel T 2015a Large area CMOS active pixel sensor x-ray imager for digital breast tomosynthesis: Analysis, modeling, and characterization *Med. Phys.* **42** 6294–308

Zhao C, Konstantinidis A C, Zheng Y, Anaxagoras T, Speller R D and Kanicki J 2015b 50 μ m pixel pitch wafer-scale CMOS active pixel sensor x-ray detector for digital breast tomosynthesis *Phys. Med. Biol.* **60** 8977–9001

Zhao W, Ristic G and Rowlands J a 2004 X-ray imaging performance of structured cesium iodide scintillators. *Med. Phys.* **31** 2594–605

Zhou J, Zhao B and Zhao W 2007 A computer simulation platform for the optimization of a breast tomosynthesis system. *Med. Phys.* **34** 1098–109